Turbulent drag reduction via adaptive surface curvature determined by flexible structural deformation

Physics of Fluids

RESEARCH ARTICLE | MARCH 12 2026

Turbulent drag reduction via adaptive surface curvature determined by flexible structural deformation

Chao Wang (王超) ; Lin Cai (蔡琳) ; Hua-Dong Yao (姚华栋) ; Guangyu Shi (时光宇); Lei Jin (金磊) ; Lucheng Sun (孙路程) ; Yuanjian Yao (姚远见); Chun Yang (杨春) ; Jianfeng Lin (林健峰) ; Chunyu Guo (郭春雨)

Physics of Fluids 38, 035131 (2026)
https://doi.org/10.1063/5.0314667

Physics of Fluids ARTICLE pubs.aip.org/aip/pof

Turbulent drag reduction via adaptive surface curvature determined by flexible structural deformation

Cite as: Phys. Fluids **38**, 035131 (2026); doi: 10.1063/5.0314667
Submitted: 1 December 2025 · Accepted: 26 February 2026 ·
Published Online: 12 March 2026

Chao Wang (王超),[1] Lin Cai (蔡琳),[1,2,a)] Hua-Dong Yao (姚华栋),[2,b)] Guangyu Shi (时光宇),[1,c)] Lei Jin (金磊),[1,d)] Lucheng Sun (孙路程),[1,e)] Yuanjian Yao (姚远见),[1,f)] Chun Yang (杨春),[1,g)] Jianfeng Lin (林健峰),[3,h)] and Chunyu Guo (郭春雨)[1,i)]

AFFILIATIONS

[1]College of Shipbuilding Engineering, Harbin Engineering University, Harbin 150001, China
[2]Division of Marine Technology, Department of Mechanics and Maritime Sciences, Chalmers University of Technology, Gothenburg 41296, Sweden
[3]The State Key Laboratory of Nonlinear Mechanics, Institute of Mechanics, Chinese Academy of Sciences, Beijing 100190, China

[a)]Electronic mail: cai_lin@hrbeu.edu.cn
[b)]Author to whom correspondence should be addressed: huadong.yao@chalmers.se
[c)]Electronic mail: guangyu.shi@hrbeu.edu.cn
[d)]Electronic mail: jin-lei@hrbeu.edu.cn
[e)]Electronic mail: heu_lucheng@hrbeu.edu.cn
[f)]Electronic mail: yyj3120870@163.com
[g)]Electronic mail: ychun0328@126.com
[h)]Electronic mail: linjf@imech.ac.cn
[i)]Electronic mail: guochunyu@hrbeu.edu.cn

ABSTRACT

Turbulent boundary layers critically influence energy consumption and performance in ships. Conventional active drag reduction methods can achieve significant resistance reduction but require high energy input and are difficult to implement at large scales, while passive techniques such as microstructured surfaces or polymer additives exhibit limited effectiveness, poor durability, and restricted environmental compatibility under practical operating conditions. Inspired by biological surfaces, this study investigates drag reduction using an adaptively deforming flexible plate in high-Reynolds-number turbulent flow. A shape-based approach is adopted: the deformation that minimizes instantaneous pressure drag and total drag is determined via two-way fluid–solid interaction and then fixed to isolate geometric effects. Since the extracted geometry corresponds to simultaneous minima of pressure drag and total drag, the fixed surface modifies the near-wall velocity gradient and wall shear, thereby reducing the frictional contribution to the total drag while maintaining pressure drag within a controllable range. These coordinated effects reorganize near-wall turbulence structures and ultimately lead to a net reduction in overall drag. These modifications reorganize near-wall turbulence structures and lead to a net reduction in wall shear stress. The results provide quantitative insights into turbulent drag reduction mechanisms and offer conceptual guidance for the development of passive surface strategies in high-Reynolds-number flows.

I. INTRODUCTION

Turbulent boundary layers are widespread in marine transportation and other engineering applications, and their characteristics play a decisive role in overall energy consumption and system performance. The turbulent boundary layer primarily generates surface shear stress (i.e., viscous frictional drag), which is typically the dominant source of resistance on streamlined bodies such as ship hulls at high Reynolds numbers. At the same time, pressure drag arises from flow separation

and geometry-induced pressure differences, and these two components jointly determine the total propulsive resistance. In marine hydrodynamics, the streamwise-developing turbulent boundary layer usually accounts for a large portion of the frictional resistance acting on a ship hull, whereas pressure drag can also become significant in certain regions or under specific operating conditions (e.g., large incidence angles or localized flow separation). The combination of the viscous shear stress and pressure distribution determines the overall drag characteristics and, consequently, has a substantial impact on fuel consumption and carbon emissions. According to the International Maritime Organization (IMO), maritime transport contributes approximately 2.9% of global CO_2 emissions, and even a 10% reduction in total drag could save millions of tons of fuel annually.[1] In the context of global carbon-neutrality objectives and regulatory measures such as the IMO's Energy Efficiency Design Index (EEDI) and Carbon Intensity Indicator (CII),[2] developing technologies capable of reducing frictional and pressure drag is of both economic and environmental significance. As a result, the pursuit of efficient, robust, and sustainable drag reduction techniques has become a critical challenge with high relevance to green and low-carbon maritime operations.[3]

Over the past several decades, a wide range of active and passive drag reduction strategies have been proposed. Active control includes wall oscillation,[4–7] suction and blowing,[8,9] synthetic jets,[10] and plasma actuation.[11–13] These methods manipulate near-wall turbulence through external energy input.[14,15] Although they can achieve significant drag reduction (up to 40% under laboratory conditions), their substantial energy consumption, control complexity, and challenges in large-scale integration hinder practical adoption in real-world marine systems.

In contrast, passive control techniques rely on geometry or material properties rather than active energy input. Classical examples include surface microstructures (riblets, dimples, and shark-skin-inspired textures),[16,17] polymers, or surfactant additives.[18] Among these, microstructured surfaces are among the most mature technologies, typically achieving 5%–10% drag reduction for moderate Reynolds numbers by restricting cross-flow motions of near-wall vortices. However, their performance deteriorates significantly under realistic ship-scale Reynolds numbers due to surface fouling, mechanical wear, and the mismatch between microstructure size and large turbulent eddies. Polymer injection[19,20] may achieve instantaneous drag reduction exceeding 50%, yet polymer chains degrade rapidly under strong shear stress, leading to short-lived effects, and the environmental risks of polymer residues remain a major concern. Overall, existing passive methods exhibit tradeoffs between effectiveness, durability, scalability, and environmental compatibility, especially under high Reynolds number turbulent conditions.

Recent advances in bio-inspired design and fluid–solid interaction (FSI) have revealed that many aquatic organisms naturally achieve efficient flow control through compliant and deformable surfaces. The flexible skins of dolphins,[21] fish scales,[22] and ray fins[23] can adapt to local pressure and shear variations, modulating near-wall turbulence, suppressing separation, and reducing drag.[24] These biological strategies have inspired the development of compliant walls and flexible structures capable of achieving passive and energy-free drag reduction. Previous studies have demonstrated that compliant surfaces can dynamically interact with the flow to modify turbulence structures.[25] Experiments by Kim and Lee[26] showed that flexible membranes can suppress quasi-streamwise vortices and yield measurable decreases in skin friction. Zhang *et al.*[27] employed coupled FSI simulations and reported up to 12% drag reduction using fish-inspired flexible surfaces. These findings highlight the potential of adaptive deformation to mitigate both frictional and pressure drag.

Despite these promising advances, several challenges remain. Most existing work focuses on idealized two-dimensional configurations or moderate Reynolds numbers, leaving the quantitative relationship between deformation magnitude and drag components (friction and pressure) insufficiently understood. Moreover, two-way FSI simulations often require substantial computational costs and raise numerical stability concerns, limiting their applicability for systematic parametric studies. These challenges motivate the development of simplified yet physically representative frameworks for analyzing how flexible surface deformation affects turbulent drag.

Motivated by these considerations, the present study investigates turbulent drag reduction using an adaptively deforming underwater flexible plate. A shape-based strategy is adopted: the optimal deformation shape with the minimum total drag coefficient is first determined using two-way FSI coupling, after which the optimal deformation is fixed to analyze its impact on the turbulent flow field and drag components. This decoupled approach isolates the effects of structural deformation from the two-way FSI process, enabling a more direct analysis of the drag reduction mechanisms associated with the geometric adaptation.

Within the present computational framework, the fluid is modeled using a three-dimensional turbulent flow solver with appropriate boundary conditions and turbulence closure models. The deformation of the flexible plate is parameterized by a dimensionless displacement amplitude $\Delta y/\delta$, which serves as the primary control variable. By systematically varying $\Delta y/\delta$, the study assesses how deformation intensity alters the flow structure, wall shear stress distribution, and pressure resistance. The goal is to establish a quantitative relationship between deformation magnitude and drag reduction effectiveness, thereby identifying scaling behaviors and adaptive flow mechanisms relevant to the design of next-generation passive drag reduction surfaces. The primary novelty of this work lies in its decoupled treatment of deformation optimization and flow-field computation in a high-Reynolds-number turbulent regime ($Re_\tau = 2000$).[28] By separating the two processes, the framework offers both computational efficiency and physical insight. Furthermore, the detailed decomposition of total drag into frictional and pressure components enables a clear identification of the mechanisms contributing to drag modification. Overall, this study provides quantitative insight into turbulence modulation induced by adaptive surface curvature. The findings deepen the understanding of how flexible surfaces interact with turbulent boundary layers and establish a conceptual foundation for future investigations of passive drag-reduction strategies in high-Reynolds-number flows.

II. COMPUTATIONAL MODEL AND METHOD

A. Computational method

1. Governing equations for fluid and solid domains

The fluid domain is solved using the improved delayed detached-eddy simulation (IDDES) based on the shear stress transport (SST) k–ω turbulence model. The governing equations are the incompressible Navier–Stokes equations. The IDDES formulation retains the same form of the continuity and momentum equations as the classical

incompressible formulation, while modifying the turbulence length scale and eddy viscosity to enable hybrid switching of the Reynolds-averaged Navier–Stokes equations (RANS) and large eddy simulation (LES).

The governing equations for incompressible flow are

$$\nabla \cdot \bar{\mathbf{u}} = 0, \tag{1}$$

$$\frac{\partial \bar{\mathbf{u}}}{\partial t} + \bar{\mathbf{u}} \cdot \nabla \bar{\mathbf{u}} = -\frac{1}{\rho}\nabla \bar{p} + \nabla \cdot [(\nu + \nu_t)\nabla \bar{\mathbf{u}}], \tag{2}$$

where $\bar{\mathbf{u}}$ is the time-averaged velocity vector, $\bar{p}$ is the pressure, ρ is the density, ν is the molecular kinematic viscosity, and ν_t is the turbulent eddy viscosity.

In the SST-based IDDES model, the turbulent viscosity is computed as

$$\nu_t = \frac{a_1 k}{\max(a_1 \omega, SF_2)}, \tag{3}$$

where k is the turbulent kinetic energy, ω is the specific dissipation rate, F_2 is a blending function, and S is the invariant measure of the strain rate.

The transport equations for k and ω are

$$\frac{\partial k}{\partial t} + \bar{\mathbf{u}} \cdot \nabla k = P_k - \beta^* k\omega + \nabla \cdot [(\nu + \sigma_k \nu_t)\nabla k], \tag{4}$$

$$\frac{\partial \omega}{\partial t} + \bar{\mathbf{u}} \cdot \nabla \omega = \alpha \frac{\omega}{k} P_k - \beta \omega^2 + \nabla \cdot [(\nu + \sigma_\omega \nu_t)\nabla \omega]. \tag{5}$$

The key feature of IDDES is the use of a modified turbulence length scale

$$l_{IDDES} = l_{RANS} - f_d \max(0,\ l_{RANS} - C_{DES}\Delta), \tag{6}$$

where l_{RANS} is the RANS characteristic length scale of the SST model, Δ is the local grid length scale, C_{DES} is a model constant, and f_d is a shielding function designed to prevent premature switching from RANS to LES in the near-wall region. Thus, the IDDES model maintains the same mathematical form as the incompressible Navier–Stokes equations, while achieving hybrid RANS–LES behavior through the modification of the turbulence length scale and eddy viscosity definition.

The solid domain is solved using a Lagrangian formulation. The governing equations include conservation of mass and conservation of linear momentum. In the Lagrangian framework, mass is strictly conserved. The mass contained in any deformed volume is equal to that contained in the corresponding undeformed reference configuration

$$\rho_0 V_0 = \rho V, \tag{7}$$

where ρ_0 and V_0 denote the density and volume in the reference configuration, respectively, and ρ and V are the density and volume in the current configuration, respectively. Thus, the density in the deformed configuration becomes

$$\rho = \frac{\rho_0 V_0}{V}. \tag{8}$$

For a linear isotropic elastic material under infinitesimal strain, the volumetric strain is expressed as

$$\frac{\Delta V}{V} = -\frac{p_m}{K}, \tag{9}$$

where K is the bulk modulus and p_m is the mean stress. The corresponding density can therefore be written as

$$\rho = \frac{\rho_0}{1 + \dfrac{\Delta V}{V}}. \tag{10}$$

The motion of the solid is governed by the Cauchy momentum equation representing conservation of linear momentum. In the Lagrangian formulation, the convective term vanishes, and the governing equation reduces to

$$\rho \frac{\partial^2 \mathbf{U}}{\partial t^2} = \nabla \cdot \boldsymbol{\sigma} + \mathbf{b}, \tag{11}$$

where $\mathbf{U}$ is the displacement vector, $\boldsymbol{\sigma}$ is the symmetric Cauchy stress tensor, and $\mathbf{b}$ is the body force per unit volume. When prescribed rigid-body rotation and translation are present, additional inertial forces are considered in the structural response.

2. IDDES turbulence modeling

Figure 1 presents the wall-normal (y^+) averaged distributions of the IDDES blending function f_d along six sampling lines (B–G). Since f_d controls the local switching between RANS and LES modes, its wall-normal variation directly reflects the spatial extent of each modeling region.

In the IDDES formulation, the hybrid length scale is constructed by modifying the wall-distance variable,

$$d_{\mathrm{IDDES}} = d - f_d \max(0, d - C_{\mathrm{DES}}\Delta), \tag{12}$$

where d is the distance to the nearest wall, C_{DES} is the DES constant, and Δ is the local grid filter width defined as

$$\Delta = V^{1/3}. \tag{13}$$

The RANS–LES separation is governed by the blending function

$$f_d = 1 - \tanh[(C_d r_d)^3], \tag{14}$$

with

$$r_d = \frac{\nu_t + \nu}{\kappa^2 d^2 S}. \tag{15}$$

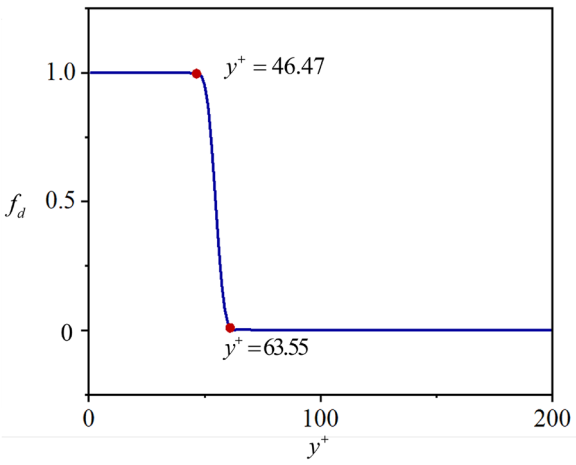

FIG. 1. Wall-normal distributions of the IDDES blending function f_d and the corresponding IDDES length scale as functions of y^+.

Here, ν_t and ν denote the eddy and kinematic viscosities, $\kappa = 0.41$ is the von Kármán constant, and S is the magnitude of the strain-rate tensor. By construction, $f_d \to 1$ enforces RANS behavior, whereas $f_d \to 0$ activates LES where the grid resolution is sufficient to resolve turbulent eddies. As shown in Fig. 1, f_d remains essentially unity for $y^+ \lesssim 46.5$ across all sampling lines, indicating that the viscous sublayer and buffer layer are fully governed by the RANS model. A rapid transition toward LES occurs only beyond $y^+ \approx 63.5$, where f_d sharply decreases toward zero. The narrow transition band between these two regions confirms that the shielding mechanism effectively prevents premature switching in the near-wall region. The consistent behavior observed along lines B–G further demonstrates that the RANS–LES interface location is insensitive to local streamwise variations, ensuring numerical robustness and modeling consistency. Consequently, the near-wall turbulence quantities analyzed in the present study—including wall shear stress and wall-normal turbulent kinetic energy—are predominantly RANS-resolved. LES is activated only in the outer boundary layer, where large-scale turbulent structures are appropriately captured. These observations confirm that the IDDES framework employed herein achieves a physically consistent zonal separation: RANS modeling accurately describes near-wall dynamics, while LES resolves energetic outer-layer turbulence without contaminating the viscous sublayer physics.

3. Fluid-structure interaction and mesh motion

A two-way strong coupling strategy was employed between the fluid and structural solvers. At each time step, fluid tractions

$$\bar{\mathbf{t}}_f = -\bar{p}\mathbf{n} + \bar{\boldsymbol{\tau}} \cdot \mathbf{n}, \tag{16}$$

were transferred to the structural solver, while the resulting displacements were mapped back to update the fluid boundary. Interface data transfer was performed using a Radial Basis Function (RBF) interpolation method with conservation correction to ensure consistency of interface work. The mesh motion satisfies

$$\nabla \cdot (\mathbf{C}_m : \nabla \mathbf{x}) = 0, \tag{17}$$

where $\mathbf{C}_m$ represents the mesh stiffness tensor, scaled according to cell size to prevent excessive distortion in refined regions. Strong coupling was achieved through sub-iterations within each time step until the relative interface residual satisfied

$$\frac{\| \mathbf{F}^k - \mathbf{F}^{k-1} \|}{\| \mathbf{F}^k \|} < 10^{-4}. \tag{18}$$

B. Model setup and boundary conditions

The computational domain is illustrated in Fig. 2. It consists of an upper fluid region and a lower solid region, coupled through an interface (interface II). A left-side sub-region in the fluid domain employs the anisotropic linear force (ALF) method to improve inlet flow stability and uniformity. By applying direction-dependent linear body forces near the inlet, the ALF region smooths the velocity transition to the main fluid domain, reducing numerical oscillations, enhancing convergence, and accelerating turbulence development. This sub-region connects to the main fluid domain via interface I. The fluid boundaries are defined as follows: the inlet and the upper surface are velocity inlets to maintain uniform flow; the outlet is a pressure outlet; the middle section and upper and lower planes are symmetry boundaries; the lower-left wall is a slip wall; and the fluid–solid interface is a no-slip wall to ensure velocity continuity. In the solid region, both ends of the bottom boundary are fixed, the middle section is a symmetry boundary, and the bottom surface is a wall. Interface II enforces the FSI coupling between the fluid and solid regions. The computational domain size is shown in Table I. The length scales are nondimensionalized with the streamwise length of the solid plate.

The computational domain adopts the Cartesian coordinate system. The origin of the coordinate system is located at the front end point of the flat plate along the plate centerline. The inflow direction is defined along the x-axis. The velocity components in the x, y, and z directions are represented by u, v, and w, respectively. In order to improve the accuracy and precision of the numerical simulation and to reduce the computational costs, the simulation is divided into a main computational domain and an ALF region. The main computational domain is further divided into four different mesh refinement regions with varying mesh resolutions. The ALF region employs a sparser mesh. The main computational domain is labeled as regions I to IV, as shown in Fig. 3. The refinement of regions I and III ensures accurate simulation of the flow in region II, while region IV is the sparsest and consistent with the ALF region. Region I extends from the inlet to the leading edge of the flat plate and uses a relatively high mesh resolution. Region II includes the fluid–solid interaction region and is assigned the highest mesh resolution to accurately capture coupled dynamics. Region III zone has a length of 0.2 after the plate and also uses a high mesh resolution, ensuring a smooth transition from the locally refined fluid–solid zone to the outlet and reducing the numerical oscillation. Region IV employs a base mesh resolution consistent with the ALF region but applies a no-slip boundary condition at the wall.

III. METHOD VALIDATION

Before proceeding with the detailed validation analyses, it is essential to outline the overall approach employed in this study to ensure the reliability and accuracy of the numerical simulations. The method validation is conducted in a stepwise manner, beginning with a grid dependency study to quantify the influence of mesh resolution on the solution. Following this, the development of turbulent structures is examined qualitatively through vortex visualization, providing insights into the flow organization and confirming the establishment

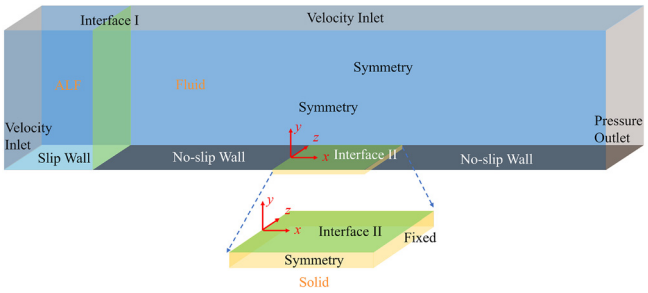

FIG. 2. The computational domain setup and relevant boundary conditions.

TABLE I. Dimensions of the sub-domains constituting the computational domain.

Sub-region	L_x	L_y	L_z
ALF	1.0	0.4	0.8
Fluid	6.0	0.4	0.8
Solid	1.0	0.4	0.01

of a fully developed turbulent state. Sections III A–III D focus on quantitative assessments, including verification of the classical logarithmic law in the near-wall region and validation of the FSI coupling. By systematically combining these analyses, a comprehensive validation of both the numerical methodology and the physical fidelity of the simulations is achieved.

A. Grid dependency and validation of the computational method

To ensure that the numerical results were independent of mesh resolution, a grid-independence study was performed using three levels of mesh density in the fluid and solid domains: medium, fine and finer. The time step was kept constant across the tests to isolate the effects of spatial discretization. Grid independence was assessed using the Grid Convergence Index (GCI) methodology of Roache.[29]

The computed quantities of C_d (the total drag coefficient) were denoted as f_1, f_2, and f_3, corresponding to the finer, fine, and medium grids, respectively. First, the monotonic convergence check is performed to satisfy the condition of $(f_3 - f_2)/(f_2 - f_1) > 0$; the sequence is monotonic; and the GCI is reliable. The representative grid spacing is h_i, and the refinement ratios are defined as

$$r_{21} = \frac{h_2}{h_1}, \quad r_{32} = \frac{h_3}{h_2}. \tag{19}$$

When only the total number of cells N_i is available for unstructured meshes, the refinement ratio can be approximated by

$$r_{21} \approx \left(\frac{N_1}{N_2}\right)^{1/d}, \quad r_{32} \approx \left(\frac{N_2}{N_3}\right)^{1/d}, \tag{20}$$

where d is the effective spatial dimension and $d = 3$ for the three-dimensional cases in this study.

TABLE II. Grid parameters.

Case	Fluid ($\times 10^6$)	Solid ($\times 10^6$)	Total ($\times 10^6$)	$\langle C_d \rangle \times 10^{-3}$	GCI	C_R
Fine	28.584	1.781	30.365	2.271	1.075%	1.005
Medium	19.078	0.640	19.718	2.295	0.487%	···
Coarse	12.500	0.320	12.820	2.306	···	···

The apparent order of the convergence p can be estimated from three grids as

$$\hat{p} = \ln\left|\frac{f_3 - f_2}{f_2 - f_1}\right| \Big/ \ln(r_{21}). \tag{21}$$

The GCI provides an estimate of the discretization uncertainty

$$\mathrm{GCI}_{12} = F_s \frac{|f_1 - f_2|}{|f_1|\left(r_{21}^{p} - 1\right)}, \quad \mathrm{GCI}_{23} = F_s \frac{|f_2 - f_3|}{|f_2|\left(r_{32}^{p} - 1\right)}, \tag{22}$$

where $F_s = 1.25$ is the safety factor recommended by Roache.[29]

The asymptotic range consistency can be verified using the ratio

$$\mathrm{C_R} = \frac{\mathrm{GCI}_{12}}{\mathrm{GCI}_{23}} r_{21}^{\hat{p}}. \tag{23}$$

If $\mathrm{C_R}$ is close to unity (typically $0.95 < \mathrm{C_R} < 1.05$), the solution is considered to be within the asymptotic convergence range. Based on the grid-independence study presented in Table II and Fig. 4, the C_d shows a monotonic convergence as the mesh is refined from medium to fine and finer grids. The GCI for the finer grid relative to the fine grid is 1.07%, and the asymptotic range consistency ratio $C_R \approx 1.005$ indicates that the solution is within the asymptotic convergence range. Therefore, the finer grid is adopted for all subsequent simulations, ensuring that the numerical results are independent of the spatial discretization while providing sufficient resolution to accurately capture fluid–solid interactions and near-wall flow features.

B. Vortex structure characterization

To validate the correct development of turbulence within the computational domain, Fig. 5 presents the three-dimensional vortex structures extracted using the Q-criterion and colored by the dimensionless streamwise velocity, which is normalized by the inlet velocity magnitude. Regions ALF and I–IV in the figure correspond to the distribution of the mesh resolutions shown in Fig. 3. Additional details

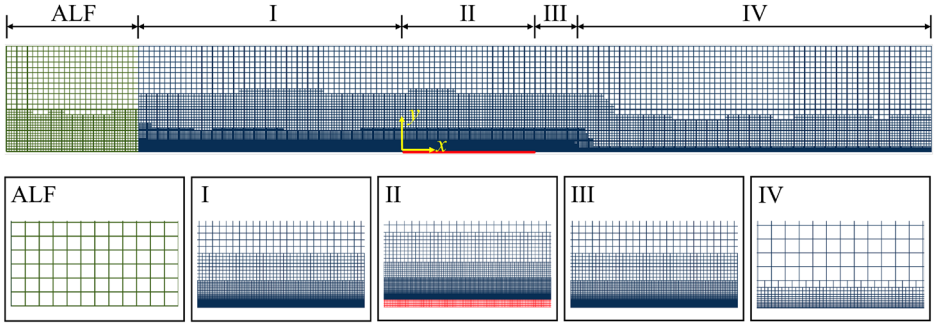

FIG. 3. Grid resolution details in the cut-plane of $y = 0$.

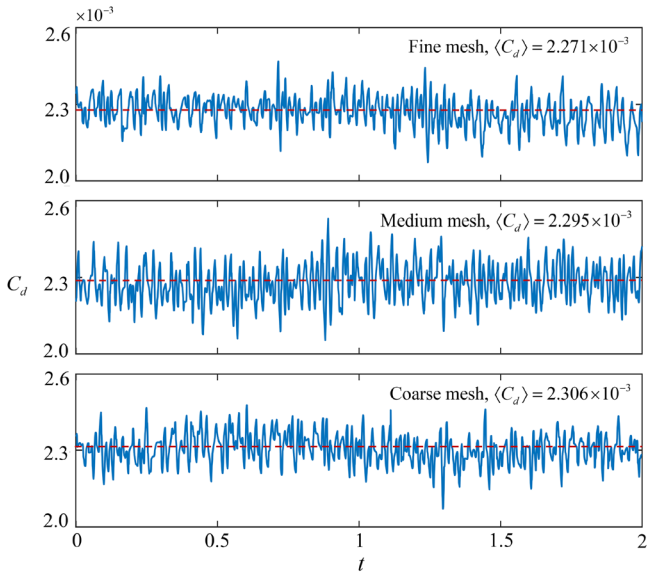

FIG. 4. Time histories of the C_d, computated from the meshes with different resolutions.

on the evolution of the vortex structure are provided in Fig. 6. This section focuses on analyzing how the mesh distribution and domain segmentation influence the vortex morphology in different streamwise regions, thereby serving as a qualitative verification of the turbulent development process.

As shown in Fig. 5, when the same $Q = 5$ is applied to both the ALF region and the main computational domain, the vortex structures in the ALF region cannot be clearly visualized. Therefore, in Fig. 6(a), a lower threshold of $Q = 0.01$ is used. Due to the relatively coarse mesh and the slip-wall boundary condition, the vortex structures in this region appear fragmented and dispersed. After the flow enters the main computational domain, the wall boundary condition changes, and in Figs. 6(b)–6(d) the mesh resolution increases along the streamwise direction. The vortex structures exhibit a clear trend toward organization, transitioning from scattered vortices to continuous, multiscale structures, with more small-scale vortices emerging near the wall. This reflects the natural adjustment of turbulence under boundary-layer shear and the available numerical resolution. As the flow approaches the downstream damping zone, the mesh becomes sparse to reduce computational cost, and this region is not relevant to the focus of the present study. Consequently, the vortex structures cannot effectively reveal the expected turbulence features, and this region is not discussed further in this work.

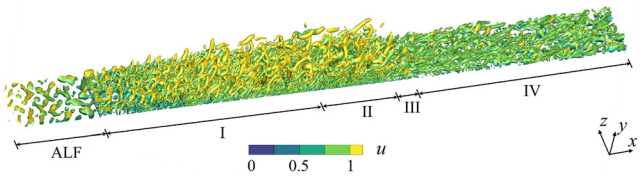

FIG. 5. Vortex visualization using Q-criterion iso-surfaces of $Q = 5$, colored by the dimensionless streamwise velocity.

Overall, the vortex structures undergo a clear streamwise evolution—from fragmentation, to organized growth, and fully developed turbulence. This evolution is highly consistent with the layout of the computational domain and mesh resolution, providing direct evidence that the simulated turbulence has reached a statistically fully developed state and establishing a solid foundation for subsequent quantitative validation.

C. Log-law verification

To further validate the simulated turbulent boundary layer, cut planes for data sampling were set at different streamwise and spanwise locations, as shown in Fig. 7. The instantaneous flow fields in these cut planes were time and space averaged in subsequent analysis.

The streamwise cut planes A–E are located at $x = -0.1$, $0.25, 0.5, 0.75, 1.1$, and the spanwise cut planes F–H at $z = 0.1$, $0.2, 0.3$. Cut-planes A–E are used to compare mean streamwise velocity profiles and boundary-layer thicknesses at different streamwise positions, while Cut-planes F–H are used to analyze spanwise flow structures. In this section, cut-planes A–E are considered.

The time-space averaged velocity profile was further analyzed for the law-of-the-wall verification. The velocity was normalized using inner scaling, $u^+ = u/u_\tau$, and the wall-normal coordinate was expressed as $y^+ = yu_\tau/\nu$. The results were compared with direct numerical simulation (DNS) data of turbulent channel flows at the friction Reynolds numbers $Re_\tau = 2000$, 950, and 550, corresponding to Hoyas and Jiménez,[30] del Álamo *et al.*,[31] and del Álamo and Jiménez,[32] respectively.

As shown in Fig. 8, the near-wall velocity profiles exhibit clear inner-layer scaling behavior. In the viscous sublayer ($y^+ < 5$), the linear relation $u^+ = y^+$ is satisfied, in agreement with theoretical predictions. In the logarithmic region ($30 < y^+ < 280$), the velocity follows the classical log-law:

$$u^+ = \frac{1}{\kappa}\ln(y^+) + B, \tag{24}$$

with the classical constants $\kappa = 0.41$ and $B = 5$. In the outer layer ($y^+ > 280$), the simulation results deviate from the DNS data, which is expected since the log-law primarily describes the inner layer dominated by the turbulent shear scale generated by the wall, u_τ. Far from the wall, the influence of the wall diminishes, and additional effects such as the wake profile and boundary layer thickness become significant, leading to the observed deviation.

These results collectively demonstrate that the simulation accurately captures the near-wall turbulence structures, the logarithmic velocity scaling, and the overall wall friction. This provides a reliable foundation for the subsequent analyses of turbulence statistics.

D. Validation of FSI coupling

To rigorously assess the accuracy and reliability of the adopted numerical method and computational grid, a benchmark case involving a flexible filament immersed in a fluid flow is considered. The computational domain for this verification is shown in Fig. 9. The problem setup follows the configuration of Huang *et al.*,[33] allowing for a direct and quantitative comparison of filament dynamics, thereby validating the present numerical implementation. In the present study, the filament is modeled at the Reynolds number $Re = 200$ and the Froude number $Fr = 0.5$. The structural material has the bending rigidity

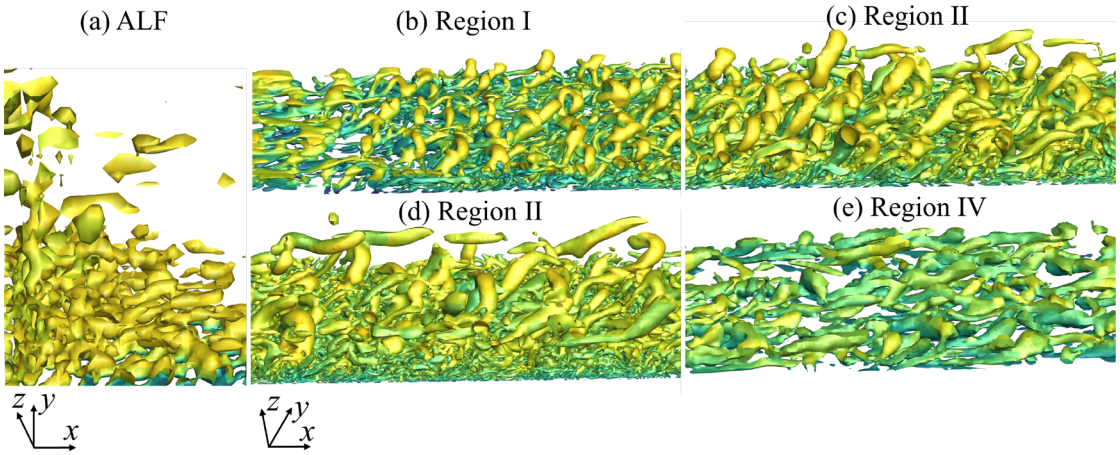

FIG. 6. Three-dimensional vortex structures in (a) the ALF region, visualized with a lower threshold of $Q = 0.01$; (b)–(e) Regions I–IV that are illustrated in Fig. 5, visualized with $Q = 5$.

$\gamma = 0.001$ and the dimensionless density $\rho = 1.5$ that is normalized based on the fluid density. The filament has a length $L = 1$ and is discretized into $N = 64$ segments. The simulation further incorporates a constant $k = 0.1\pi$ and feedback forcing coefficients $\alpha = -10^6$ and $\beta = -10^2$, with a maximum time step of $\Delta t = 0.0003$.

Figure 10 presents the temporal evolution of the filament obtained from the present simulations alongside the reference results from Huang *et al.*[33] The dimensionless amplitude y and time t are normalized by the filament length and the time required for the flow to traverse the entire filament, respectively. Agreement is observed in deformation patterns, indicating that the numerical method accurately captures the fluid–solid interactions. Minor discrepancies are within the expected numerical tolerance and do not compromise the overall fidelity of the simulations.

These results confirm the accuracy and applicability of the adopted numerical methodology. The close agreement with established benchmark data demonstrates that the approach is suitable for simulations of flexible structures in fluid flows, providing a reliable foundation for subsequent investigations of fluid–solid interaction phenomena.

IV. RESULTS AND DISCUSSION

A. Parametric analysis of flexible plate deformation

Before analyzing the deformation characteristics, it is necessary to clarify the numerical strategy adopted in this study. During the initial two-way FSI simulations, it was observed that continuous vibration of the flexible plate did not lead to a net drag reduction effect. As shown in Fig. 11, to further investigate the underlying mechanisms, the total drag coefficient C_d, was decomposed into the skin friction coefficient, C_f, and the pressure-drag coefficient, C_p.

To quantitatively evaluate the performance, the drag reduction rate (DR) is defined as the relative difference in the total drag coefficient between the baseline rigid-wall case and the FSI case, normalized by the baseline value

$$DR = \frac{\langle C_{d,\text{rigid}} \rangle - \langle C_{d,\text{flexible}} \rangle}{\langle C_{d,\text{rigid}} \rangle} \times 100\%, \tag{25}$$

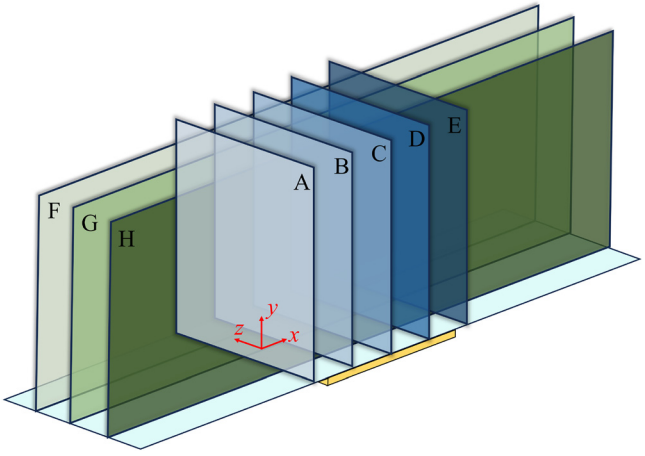

FIG. 7. Schematic of the cut-planes for data sampling inside the computational domain.

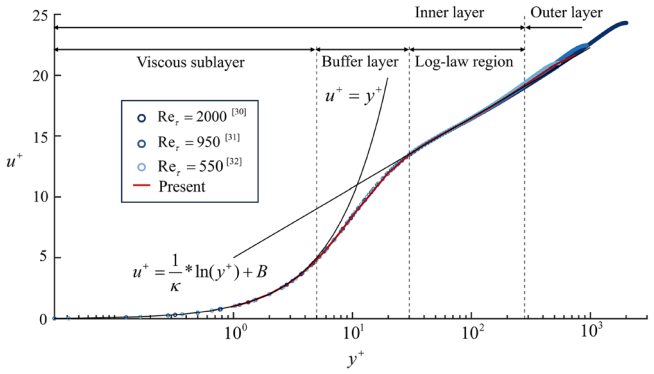

FIG. 8. Scaled mean velocity profiles, u^+ vs y^+, compared with the DNS data from Hoyas and Jiménez,[30] del Álamo *et al.*,[31] and del Álamo and Jiménez.[32]

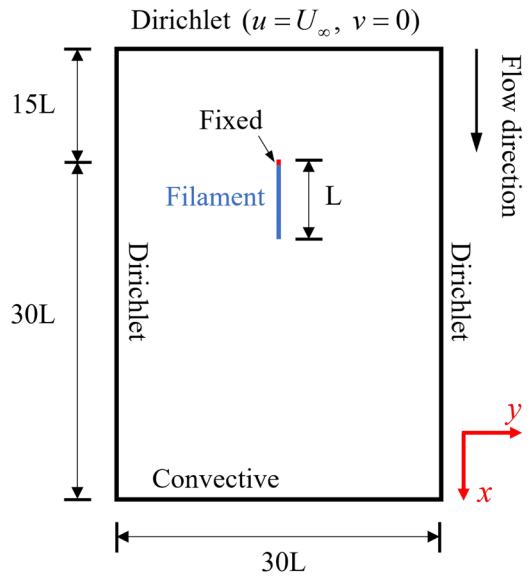

FIG. 9. Numerical model of the flexible filament used for the verification of the FSI coupling method.

where $C_{d,\text{rigid}}$ and $C_{d,\text{flexible}}$ are the time-averaged total drag coefficients of the rigid-wall and flexible-plate cases, respectively; and $\langle\cdot\rangle$ denotes the time-averaging operator. A positive DR value indicates effective drag reduction.

These quantities were compared between the FSI case and the corresponding baseline rigid-wall case in Table III. The calculated DR value of -31.63% for the total drag quantitatively confirms the absence of a net drag-reduction benefit in the continuously vibrating case. It is observed that the C_f shows a slight decrease compared to the rigid wall, while the C_p exhibits a significant increase, collectively resulting in a net drag increase in the continuously vibrating case.

Observed from the results, the flexible plate with specific material properties reaches a transient state where both the C_p and C_d attain local minimum values, as indicated by point A in Fig. 11. The vertical axis represents the normalized wall-normal displacement, $\Delta y/\delta$, where δ denotes the velocity boundary layer thickness at the middle streamwise location of the plate. The wall-normal deformation represents the relative amplitude of plate deformation with respect to the local boundary-layer thickness. All instances of time t in this study are

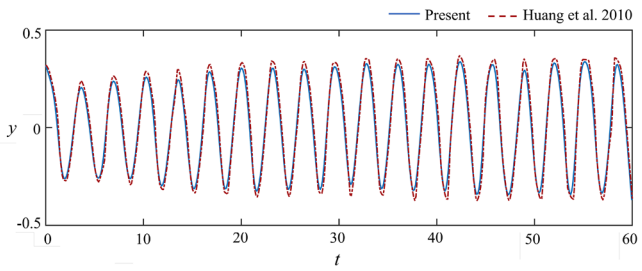

FIG. 10. Displacement of the free end of the flexible filament changes with time, compared with the simulation results by Huang *et al.*[33]

TABLE III. Drag coefficients of the continuously vibrating FSI case and the rigid-wall baseline.

Case	$\langle C_d\rangle \times 10^{-3}$	$\langle C_f\rangle \times 10^{-3}$	$\langle C_p\rangle \times 10^{-3}$
Flexible plate	2.990	2.214	0.776
Rigid wall	2.271	2.271	0.0
DR (%)	−31.633	2.525	···

nondimensionalized based on the time required for the flow to pass over the entire plate. The streamwise distance x is nondimensionalized based on the plate streamwise length. During the vibration process, there are trough states where the flexible plate adapts to the local turbulence, thereby minimizing the total drag at that specific instant. Motivated by this observation, the instantaneous geometry of the flexible plate at Point A was extracted and fixed as a static shape for subsequent simulations. The flow around this optimized plate shape was then re-simulated under identical turbulent inflow conditions. Results demonstrate that this optimized shape achieves a significant drag reduction effect compared to both the continuously vibrating case and the rigid-wall case, which will be elaborated in detail in Sec. IV A 1.

1. Deformation effects on drag coefficients

Although the optimized flexible surface shape obtained through the above procedure exhibits a preliminary drag-reduction effect, it cannot be asserted that this configuration represents the most optimal drag-reducing geometry. Therefore, an additional series of simulations was conducted to quantitatively analyze the influence of surface deformation on the drag components. In order to identify a potentially more effective drag-reducing configuration within a reasonable range of deformation amplitudes, different surface states were selected during the two-way FSI simulations. These surface shapes correspond to the various geometries that arise under realistic physical conditions.

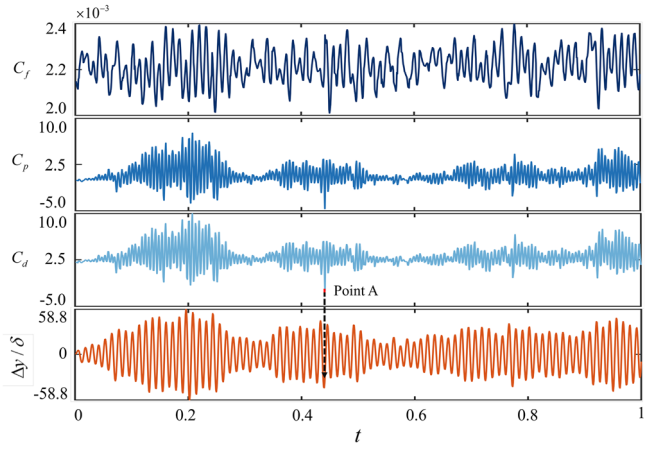

FIG. 11. Time history of the total drag coefficient C_d, the friction drag component C_f, the pressure-drag component C_p, and the normalized plate displacement $\Delta y/\delta$ for the continuously vibrating flexible plate in the initial two-way FSI analysis. The time is normalized with the period of the flow passing over the plate.

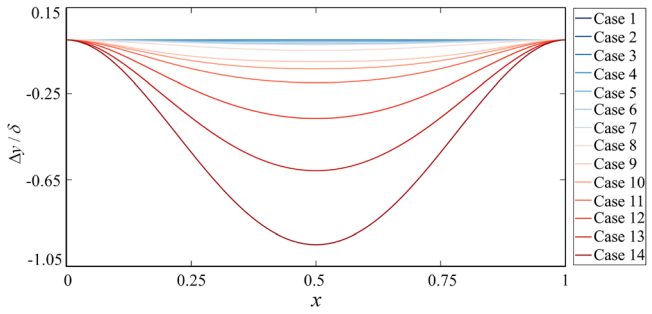

FIG. 12. Nondimensional wall-normal displacement for the parametric cases.

Based on the surface adaption, 14 cases were constructed. Figure 12 displays the normalized wall-normal displacement curves of the plate along the streamwise direction in these cases. Here the two-dimensional curves are shown, since the displacements are the same along the spanwise direction, which is related to the spanwise periodic boundary condition of the structure. The figure shows the geometric variation from small to large deformation amplitudes. The values are always negative, which correspond to deformations in the negative y-direction. The maximum magnitudes, Δy_{max}, appear at the middle point of the plate; and $-\Delta y_{max}/\delta$ are listed in Table IV.

Figure 13 summarizes the mean drag coefficients, $\langle C_d \rangle$, $\langle C_f \rangle$, and $\langle C_p \rangle$, under different maximum wall-normal deformation amplitudes. It reveals a clear scale-dependent response with respect to the boundary layer thickness δ. The Gaussian curve fitting (GCF) based on a Gaussian-kernel smoothing method is employed to extract the underlying trend from the discrete drag-coefficient data that are the raw results obtained directly from the simulations. For the original data points $\{(x_i, y_i)\}_{i=1}^{N}$, the smoothed value at any location x is obtained through a weighted averaging process that is formulated as

$$\tilde{y}(x) = \frac{\sum_{i=1}^{N} y_i \exp\left[-\frac{(x_i - x)^2}{2\sigma^2}\right]}{\sum_{i=1}^{N} \exp\left[-\frac{(x_i - x)^2}{2\sigma^2}\right]}, \tag{26}$$

where σ is the standard deviation of the Gaussian kernel and controls the degree of smoothing. In this study, $\sigma = 0.65$ is adopted, which effectively filters local fluctuations while preserving the overall trend of the data. Therefore, the GCF curves represent the dominant

TABLE IV. Deformation magnitudes for the self-adaptive drag reduction.

Case index	$-\Delta y_{max}/\delta$	Case index	$-\Delta y_{max}/\delta$
1	1.112×10^{-5}	8	4.882×10^{-2}
2	2.824×10^{-5}	9	9.941×10^{-2}
3	1.488×10^{-4}	10	1.326×10^{-1}
4	1.644×10^{-3}	11	1.952×10^{-1}
5	8.382×10^{-3}	12	3.588×10^{-1}
6	1.665×10^{-2}	13	5.971×10^{-1}
7	2.200×10^{-2}	14	9.324×10^{-1}

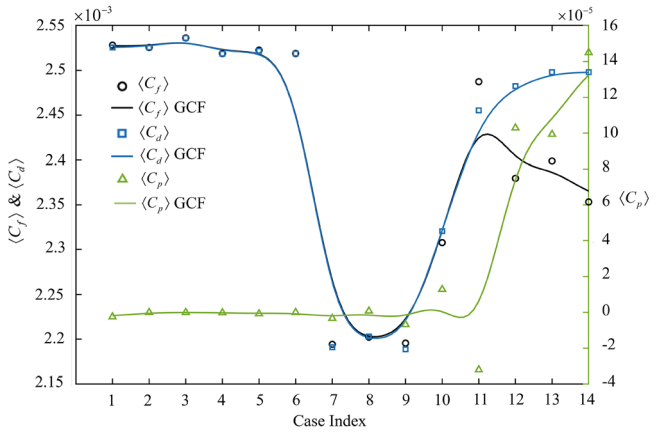

FIG. 13. Distribution and trends of the mean drag coefficients across case indices. Discrete markers denote actual measured values, while curves illustrating their underlying trends are generated using the Gaussian curve fitting (GCF). The total drag coefficient $\langle C_d \rangle$ and the friction-drag coefficient $\langle C_f \rangle$ are plotted against the left y-axis, and the pressure-drag coefficient $\langle C_p \rangle$ against the right y-axis.

variation of the drag components as a function of the deformation amplitude.

Three distinct regimes with weak, intermediate and strong deformations can be quantitatively identified. In the weak-deformation regime ($\Delta y/\delta \lesssim 10^{-2}$), the wall-normal deformation is much smaller than the boundary-layer thickness, and the flow barely perceives the geometric disturbance; thus, both C_f and C_p remain nearly constant, and the drag variation is minimal, with the surface behaving effectively as a rigid flat plate. In the intermediate-deformation regime ($10^{-2} \lesssim \Delta y/\delta \lesssim 10^{-1}$), the deformation amplitude is sufficient to modify the near-wall shear distribution but is not large enough to induce local separation. As a result, C_f decreases noticeably, while C_p remains within a controllable range without significant amplification. The combined effect of a pronounced reduction in skin-friction drag and the maintenance of pressure drag at a moderate level jointly leads to the minimum total drag coefficient C_d in this regime, indicating that drag reduction arises from a coordinated balance between frictional attenuation and pressure stabilization rather than from a single dominant contribution. In the strong-deformation regime ($\Delta y/\delta \gtrsim 10^{-1}$), when the deformation amplitude approaches or exceeds the boundary-layer thickness, the beneficial drag-reduction mechanisms gradually saturate or even reverse. Excessive geometric protrusions enhance adverse pressure gradients, causing C_p to rise significantly, while the increased curvature also leads to a rise in C_f, and consequently, C_d increases again. Among all the parametric deformation cases, cases 7–9 approach the optimal deformation range for maximizing drag reduction while avoiding performance recovery under strong deformation conditions. This range achieves the best balance between reducing surface frictional resistance and avoiding additional pressure damping. Since these three cases show no deviation in drag reduction performance, case 9 will be analyzed in the later sections to reveal the instantaneous physical mechanism of the adaptive drag reduction effect.

2. Determination of optimal curvature

Through quantitatively analyzing the trends of the C_f, C_p, and C_d under the different deformation amplitudes, surface geometries that

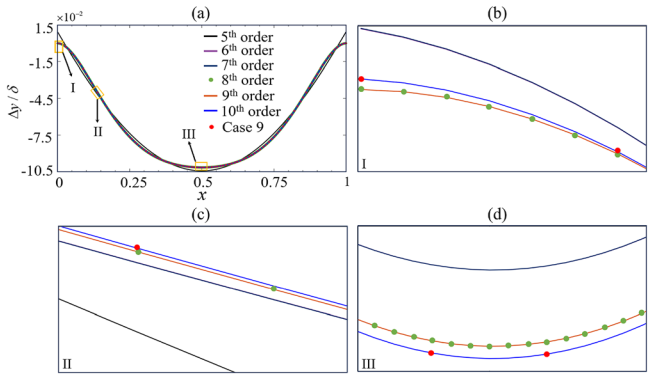

FIG. 14. (a) Fitting polynomials at different orders. The three yellow boxes, I, II, and III, represent magnified areas, corresponding to (b)–(d), respectively.

exhibit enhanced drag-reduction performance are identified, from which the fundamental principles governing effective drag-reduction configurations are further extracted. A high-order polynomial fitting is then employed to obtain the mathematical representation of the surface profiles corresponding to the drag-reducing geometries.

Figure 14 compares the surface shape of the optimal drag reduction configuration with curves fitted at different orders. The results show that the tenth order perfectly matches the optimal drag-reducing surface shape curve. Meanwhile, Table V presents the coefficients of the fitting polynomials of different orders. The analytical expression can be written as

$$\frac{\Delta y}{\delta} = -\sum_{i=0}^{n} a_i x^i, \tag{27}$$

where a_i is the polynomial coefficient.

The fitting results of different order fitted curves and simulated curves show that the adaptive deformation of the flexible plate follows a smooth deterministic law, which can be accurately described by an tenth-order polynomial. This analytical method provides valuable guidance for the parametric design and optimization of flexible turbulent adaptive drag-reducing surfaces.

B. Flow structure comparison and drag reduction mechanism

The surface configuration that minimizes the pressure drag is systematically determined, and this optimal deformation is accurately captured through high-order polynomial fitting, thus providing a concise mathematical representation of the most effective surface shape. Based on this optimized surface configuration, this section will study the relevant flow structure and drag reduction mechanism in detail.

1. Boundary layer development

Figure 15 compares the mean streamwise velocity profiles at cut-planes A–E (refer the locations to Fig. 7), together with the profile obtained by averaging these cut-planes. The vertical axis represents the dimensionless streamwise velocity $\langle u \rangle$, and the horizontal axis denotes the wall-normal coordinate y^+. The red curves correspond to the straight rigid wall (SRW), whereas the blue curves represent the drag-reducing surface (case 9).

The observation reveals that across all streamwise locations, the boundary layer thickness δ of case 9 consistently exceeds that of SRW, indicating that the drag-reducing surface leads to a thicker boundary layer. This thickening is generally associated with reduced wall-shear stress, where the weakened near-wall velocity gradient implies lowered skin friction. The modest elevation of the case 9 velocity in the buffer/logarithmic region suggests that the optimized surface alters near-wall turbulence production or modifies the local velocity gradient to achieve drag reduction. Although the individual cut-planes exhibit slight local variations, the averaged profile remains smooth and preserves the systematically increased boundary-layer thickness of case 9.

2. Vorticity field

As shown in Fig. 16, the near-wall vorticity intensity in case 9 (the drag-reducing surface) is generally lower than that in SRW (the straight rigid wall). For all three vorticity components (ω_x, ω_y, ω_z) and the total magnitude $|\omega|$, the small-scale and high-frequency vortical structures are significantly weakened or even absent in case 9, while SRW exhibits densely packed, fine vortical structures near the wall.

For the streamwise component ω_x, SRW shows elongated streak-like vortical bands aligned with the flow direction, which represent the classical near-wall quasi-streamwise vortices responsible for turbulence regeneration. In contrast, these vortical bands in case 9 become much less distinct and more spatially sparse, suggesting a suppression of the formation and maintenance of near-wall streak–vortex pairs. The wall-normal component ω_y in SRW exhibits frequent alternations of positive and negative regions, reflecting intense ejection and sweep motions that continuously generate wall-normal rotation. In case 9, ω_y becomes weaker and smoother, indicating that the vertical motion and associated shear-induced vortices are effectively reduced. Similarly, the spanwise

TABLE V. The coefficients of the fitting polynomials at the different orders.

Order	a_{10}	a_9	a_8	a_7	a_6	a_5	a_4	a_3	a_2	a_1	a_0
10	−0.3543	1.7711	−3.6367	3.9210	−2.0376	−0.1739	0.9428	−0.5626	0.1300	0.0000	0.0000
9	⋯	−0.0003	0.1393	−0.5542	1.1873	−1.6251	1.3460	−0.6284	0.1356	−0.0002	0.0000
8	⋯	⋯	0.1380	−0.5518	1.1848	−1.6236	0.1380	−0.6283	0.1356	−0.0002	0.0000
7	⋯	⋯	⋯	0.002	0.2831	−0.8508	0.9738	−0.5292	0.1221	0.0006	0.0000
6	⋯	⋯	⋯	⋯	0.2840	−0.8519	0.9747	−0.5295	0.1222	0.0006	0.0000
5	⋯	⋯	⋯	⋯	⋯	0.0001	0.0065	−0.0131	−0.0069	0.0135	−0.0003

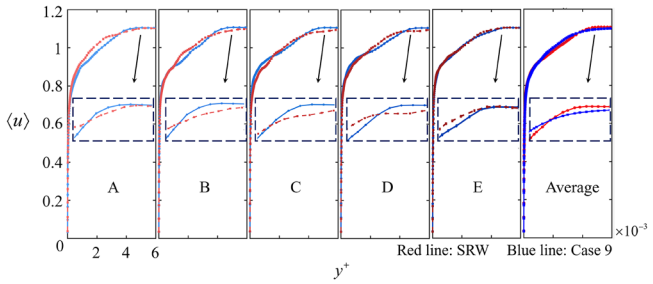

FIG. 15. Profiles of the mean streamwise velocity $\langle u \rangle$ as function of the wall-normal coordinate y^+ in cut-planes A–E. The red curves represent the SRW, and the blue curves correspond to case 9.

component ω_z in SRW contains rich small-scale fluctuations related to spanwise instabilities and streak breakdown, while case 9 shows weaker and larger-scale ω_z structures, suggesting a stabilization of spanwise shear layers.

Overall, the vorticity magnitude $|\omega|$ distribution confirms that the near-wall region of SRW is dominated by strong, small-scale vortices, whereas case 9 displays reduced vorticity peaks and fewer localized high-vorticity cores, implying a smoother, more coherent flow structure in the near-wall zone.

3. Energy transmission

Figure 17 presents the comparison of turbulent kinetic energy (k) between the smooth rigid wall (SRW) and the optimized drag-reducing surface (case 9). Instantaneous contour fields are shown together with quantitative profiles extracted along representative streamwise (b–d) and spanwise (e–g) cut-lines.

The contour plots indicate noticeable differences in the spatial organization of turbulent kinetic energy. In SRW, high-k regions appear in fragmented and densely distributed patches near the wall, reflecting strong small-scale turbulence activity. In contrast, case 9 exhibits a redistribution of k, with altered spatial coherence and modified near-wall structures.

Quantitative comparisons reveal that the averaged k values along the streamwise cut-lines are consistently higher in case 9 than in SRW, whereas along the spanwise cut-lines, the averaged k values are lower. This indicates that the optimized surface does not uniformly reduce turbulent kinetic energy; instead, it induces an anisotropic redistribution of turbulence intensity in the near-wall region.

The increase in k along the streamwise direction suggests enhanced streamwise-aligned structures or elongated coherent motions, while the reduction along the spanwise direction implies suppression of lateral turbulent fluctuations. Such directional reorganization modifies the turbulence structure without necessarily reducing the total energy content uniformly.

Therefore, the drag-reduction mechanism in case 9 should be interpreted as a structural reorganization of near-wall turbulence rather than a simple global attenuation of turbulent kinetic energy. The adaptive surface curvature redistributes energy preferentially along the streamwise direction while weakening spanwise turbulent activity, leading to a modified shear distribution and altered wall-shear characteristics. This anisotropic modulation of turbulence plays a key role in the observed drag modification.

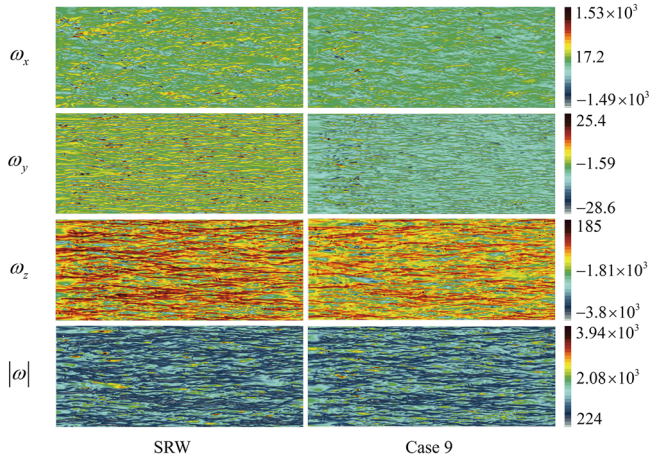

FIG. 16. Instantaneous vorticity contours of SRW (left) and case 9 (right). From top to bottom: streamwise vorticity ω_x, wall-normal vorticity ω_y, spanwise vorticity ω_z, and total vorticity magnitude $|\omega|$.

4. Wall shear stress

Figures 18–20 present comparisons of the instantaneous wall shear stress between SRW and case 9, including the total magnitude $|\tau|$, the streamwise component τ_x, and the spanwise component τ_z, respectively. Each figure contains the corresponding contour distributions together with line-averaged values extracted along six representative cut-lines (b–d in the streamwise direction and e–g in the spanwise direction). The wall-normal component τ_y is negligible and therefore omitted.

As shown in Fig. 18, SRW exhibits densely distributed high-intensity shear regions near the wall, characterized by fine-scale and spatially fragmented structures. In case 9, the high-shear cores become more spatially organized, particularly in the downstream region. The line-averaged results indicate that the mean value of $|\tau|$ in case 9 is lower than that of SRW only along the downstream cut-line d, while along b, c, e, f, and G the averaged magnitude is comparable to or slightly higher than that of SRW. This demonstrates that drag reduction is not associated with a uniform attenuation of local shear stress intensity.

Figure 19 shows that SRW is dominated by elongated streak-like τ_x structures aligned with the flow direction, reflecting strong near-wall velocity gradients and momentum transfer. In case 9, these streaks become less clustered and more spatially redistributed. Consistent with the magnitude results, the averaged τ_x is reduced relative to SRW only at cut-line d, while at other sampling locations it exhibits similar or slightly larger values. This indicates that the streamwise shear stress contribution is redistributed rather than globally suppressed.

As shown in Fig. 20, SRW presents rich small-scale variations of τ_z, associated with spanwise momentum exchange and near-wall streak instabilities. In case 9, these fluctuations appear smoother and more coherent in the downstream region. The averaged results reveal reductions of τ_z along cut-lines c and f, whereas other sections show comparable or moderately increased values relative to SRW. This further confirms that the effect of the optimized surface is spatially non-uniform.

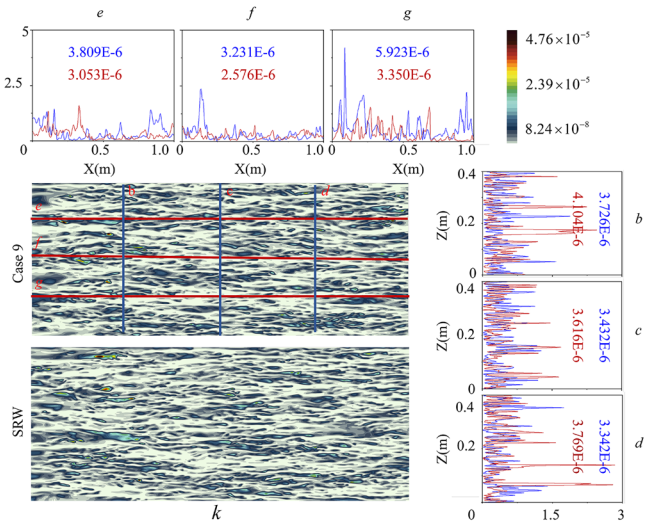

FIG. 17. Comparison of turbulent kinetic energy (k) between SRW and case 9. Each profile plot contains a set of numerical values: the blue numbers denote the line-averaged values of case 9 along the corresponding cut-line, while the red numbers represent the line-averaged values of SRW along the same cut-line.

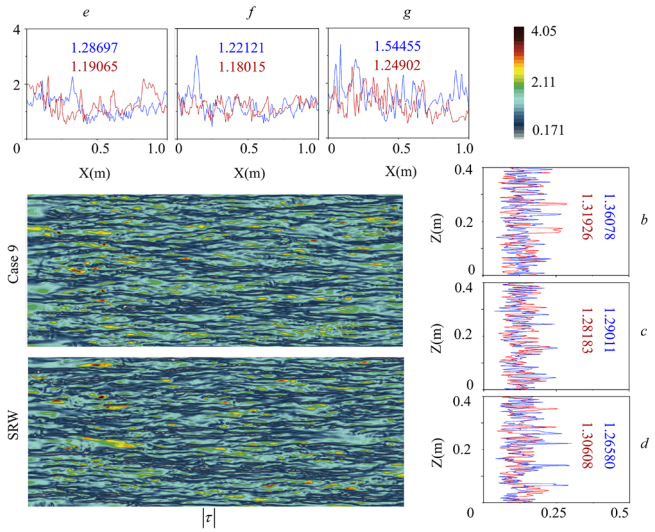

FIG. 18. Comparison of wall shear stress magnitude $|\tau|$ between SRW and case 9. The upper panels show instantaneous contour distributions, and the lower panels present line-averaged values along streamwise cut-lines and spanwise cut-lines.

Although the line-averaged wall shear stress components do not decrease monotonically at all sampling locations, drag reduction does not require uniform local suppression. The skin-friction drag coefficient is governed by the surface-integrated mean wall shear stress,

$$C_f = \frac{1}{\frac{1}{2}\rho U_\infty^2 A}\int_A \bar{\tau_w}\, dA, \tag{28}$$

where

$$\tau_w = \mu \frac{\partial U}{\partial y}\bigg|_{y=0}. \tag{29}$$

Therefore, the net friction drag depends on the area-integrated distribution of τ_w. Even if local increases occur in certain upstream or lateral regions, a global reduction can still arise provided that the decreases in dynamically dominant regions (such as the downstream zone) produce a larger negative contribution to the integral

$$\Delta C_f \propto \int_A \Delta\tau_w\, dA. \tag{30}$$

It is important to emphasize that the optimized surface geometry was obtained through instantaneous pressure-drag minimization in the two-way fluid–structure interaction framework. Although the optimization targeted pressure drag, the resulting curvature modifies the near-wall velocity gradients and reorganizes turbulence structures. This geometric effect redistributes the spatial contributions of τ_x, τ_z, and $|\tau|$, particularly attenuating high-shear regions in the downstream area, thereby reducing the surface-integrated skin-friction drag. Consequently, the total drag reduction observed in case 9 arises from a coupled mechanism: direct pressure-drag minimization during shape extraction and subsequent redistribution of near-wall shear stress after the geometry is fixed. The results indicate that drag mitigation is achieved through spatial reorganization of momentum transfer rather than through uniform attenuation of shear stress intensity.

5. Drag reduction mechanism

The drag reduction observed in case 9 originates from a systematic restructuring of the near-wall turbulence induced by the optimized surface curvature. Relative to SRW, the boundary layer becomes consistently thicker and the mean velocity gradient at the wall is moderated, indicating a redistribution of momentum exchange within the near-wall region rather than a simple attenuation of flow intensity.

This modification of the mean profile is accompanied by a marked reduction in fragmented, small-scale vortical structures. The densely packed quasi-streamwise vortices and shear-layer instabilities characteristic of SRW are replaced by smoother and more spatially coherent motions, suggesting a stabilization of the near-wall dynamical organization. The turbulent kinetic energy field reflects the same trend: instead of exhibiting uniformly reduced magnitude at every sampling location, the optimized surface redistributes turbulent activity, suppressing concentrated high-energy patches and reducing structural intermittency in the near-wall layer.

The wall shear stress distributions confirm that drag reduction results from spatial reallocation rather than monotonic local decrease. Although certain sections show localized increases in individual components, the downstream and energetically dominant regions display clear attenuation, leading to a net reduction in the surface-integrated shear stress. Notably, the geometry extracted through instantaneous pressure-drag minimization modifies the near-wall velocity gradients once fixed, thereby simultaneously reducing both pressure-related contributions and frictional resistance.

In essence, the optimized surface does not eliminate turbulence; it reorganizes it. By stabilizing coherent motions, reducing localized high-shear concentrations, and redistributing turbulent kinetic energy within the boundary layer, the adaptive curvature produces a lower

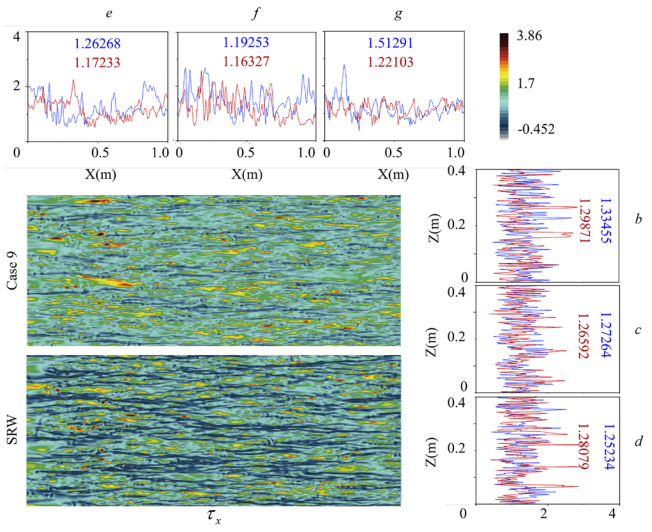

FIG. 19. Comparison of streamwise wall shear stress component τ_x between SRW and case 9. The upper panels show instantaneous contour distributions, and the lower panels present line-averaged values along the selected cut-lines.

wall-integrated drag. The mechanism can therefore be characterized as turbulence redistribution and boundary-layer reorganization driven by flow-induced geometric adaptation.

V. CONCLUSIONS

The study first carried out comprehensive qualitative and quantitative validation of the turbulent boundary layer. Three-dimensional vortex structures visualized via the Q-criterion reveal dense vortex structures and multi-scale organizations near the wall where the adaptive structural surface is positioned (region II), exhibiting fully developed turbulent characteristics. The mean velocity profiles in inner

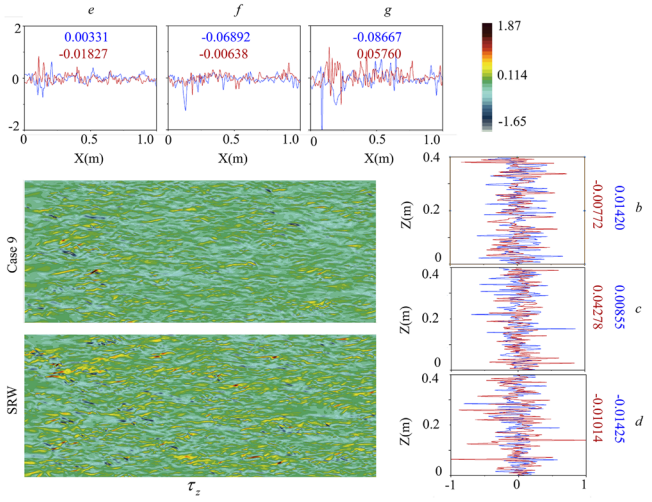

FIG. 20. Comparison of spanwise wall shear stress component τ_z between SRW and case 9. The upper panels show instantaneous contour distributions, and the lower panels present line-averaged values along the selected cut-lines.

scaling satisfy the linear viscous sublayer relation and the logarithmic law in the near-wall region, consistent with reference DNS data.

Next through two-way FSI simulations, it was found that continuous vibration of the flexible plate alone does not produce net drag reduction. So the central premise of this work is that fixing deformation shapes extracted from instantaneous drag minima allows the geometric effect to be isolated from fluid–structure coupling. Importantly, this premise is not presupposed but systematically validated. We observed that pressure drag dominates the total drag and that instantaneous minima of pressure drag coincide with minima of total drag. Based on this observation, the corresponding surface shapes were extracted and imposed as static geometries under a stationary flow field. The results indicate that, once coupling effects are removed, drag reduction is not universal: only deformation amplitudes within a specific wall-normal range lead to a net decrease in total drag. This confirms the conditional validity of the geometric-isolation hypothesis for the plate configurations studied. Then the optimal configuration was accurately captured using a high-order polynomial fit, providing an analytical expression for the self-adaptive surface profile.

Detailed flow field analysis reveals that the drag reduction mechanism is related to the systematic reconstruction of near-wall turbulence. Compared to a straight, rigid wall, the optimized surface produces a thicker boundary layer and mitigates the mean velocity gradient at the wall. The fragmentation of the near-wall vortex field is reduced, the concentration of small-scale, high-strength structures decreases, and spatial coherence is enhanced. Although the turbulent kinetic energy and wall shear stress components do not decrease uniformly at every sampling point, their spatial distribution undergoes significant reorganization. The increase in local regions is offset by the reduction in dynamically dominant regions, ultimately leading to a net reduction in the surface integral wall shear stress. Since the extracted geometry is derived from minimizing instantaneous pressure drag and total drag, the fixed surface that ultimately produces the drag reduction effect simultaneously alters the near-wall velocity gradient and wall shear, thereby reducing the contribution of frictional drag to the total drag and keeping pressure drag within a controllable range.

In summary, the optimized flexible surface achieves drag reduction not through a global attenuation of turbulence intensity, but through redistribution of turbulent kinetic energy, stabilization of coherent near-wall structures, and reorganization of wall shear stress. More broadly, the study provides a validated framework for distinguishing geometric modulation effects from fluid–structure coupling effects in adaptive-wall systems, clarifying that geometry-driven drag reduction is amplitude-dependent rather than an inherent consequence of structural vibration. The results provide quantitative insight into turbulence–geometry interaction mechanisms and offer a physically grounded framework for the design of adaptive passive drag-reduction surfaces in high-Reynolds-number flows.

ACKNOWLEDGMENTS

This work was supported by the National Natural Science Foundation of China (Project No. U25A20376) and the National Key Laboratory of Hydrodynamics. The work was also supported by the project "3D Virtual Platform for Digitalization of Holistic Acoustic Environment in Cabs of Heavy-Duty Vehicles (OCTAVE)" (Grant No. P2024-01011) in the VINNOVA Strategic Vehicle Research and Innovation Program from the Swedish Energy Agency. The

computations and data handling were enabled by resources provided by the National Academic Infrastructure for Supercomputing in Sweden (NAISS), partially funded by the Swedish Research Council through Grant Agreement No. 2022-06725.

AUTHOR DECLARATIONS

Conflict of Interest

The authors have no conflicts to disclose.

Author Contributions

Chao Wang: Funding acquisition (equal); Methodology (equal); Project administration (equal); Resources (equal); Supervision (equal). **Lin Cai:** Conceptualization (equal); Data curation (equal); Formal analysis (equal); Investigation (equal); Methodology (equal); Validation (equal); Visualization (equal); Writing – original draft (equal). **Hua-Dong Yao:** Formal analysis (equal); Funding acquisition (equal); Methodology (equal); Project administration (equal); Resources (equal); Software (equal); Supervision (equal); Writing – review & editing (equal). **Guangyu Shi:** Investigation (equal); Methodology (equal); Project administration (equal); Supervision (equal). **Lei Jin:** Investigation (equal); Methodology (equal); Validation (equal). **Lucheng Sun:** Investigation (equal); Methodology (equal); Visualization (equal). **Yuanjian Yao:** Investigation (equal); Methodology (equal); Validation (equal). **Chun Yang:** Investigation (equal); Methodology (equal); Visualization (equal). **Jianfeng Lin:** Investigation (equal); Methodology (equal); Validation (equal). **Chunyu Guo:** Funding acquisition (equal); Project administration (equal); Resources (equal); Supervision (equal).

DATA AVAILABILITY

The data that support the findings of this study are available from the corresponding author upon reasonable request.

REFERENCES

[1]M. Reche-Vilanova, H. Hansen, and H. B. Bingham, "Performance prediction program for wind-assisted cargo ships," J. Sailing Technol. **6**, 91–117 (2021).
[2]M. Bayraktar and O. Yuksel, "A scenario-based assessment of the energy efficiency existing ship index (EEXI) and carbon intensity indicator (CII) regulations," Ocean Eng. **278**, 114295 (2023).
[3]P. R. Spalart and J. D. McLean, "Drag reduction: Enticing turbulence, and then an industry," Philos. Trans. R. Soc., A **369**, 1556–1569 (2011).
[4]K.-S. Choi, J.-R. DeBisschop, and B. R. Clayton, "Turbulent boundary-layer control by means of spanwise-wall oscillation," AIAA J. **36**, 1157–1163 (1998).
[5]K.-S. Choi and B. R. Clayton, "The mechanism of turbulent drag reduction with wall oscillation," Int. J. Heat Fluid Flow **22**, 1–9 (2001).
[6]K.-S. Choi, "Near-wall structure of turbulent boundary layer with spanwise-wall oscillation," Phys. Fluids **14**, 2530–2542 (2002).
[7]J.-I. Choi, C.-X. Xu, and H. J. Sung, "Drag reduction by spanwise wall oscillation in wall-bounded turbulent flows," AIAA J. **40**, 842–850 (2002).
[8]J. H. Fransson, P. Konieczny, and P. H. Alfredsson, "Flow around a porous cylinder subject to continuous suction or blowing," J. Fluids Struct. **19**, 1031–1048 (2004).
[9]L. Huang, P. Huang, R. LeBeau, and T. Hauser, "Numerical study of blowing and suction control mechanism on NACA0012 airfoil," J. Aircr. **41**, 1005–1013 (2004).
[10]A. Glezer, "Some aspects of aerodynamic flow control using synthetic-jet actuation," Philos. Trans. R. Soc., A **369**, 1476–1494 (2011).
[11]O. Mahfoze and S. Laizet, "Skin-friction drag reduction in a channel flow with streamwise-aligned plasma actuators," Int. J. Heat Fluid Flow **66**, 83–94 (2017).
[12]F. Thomas, T. Corke, A. Duong, S. Midya, and K. Yates, "Turbulent drag reduction using pulsed-DC plasma actuation," J. Phys. D: Appl. Phys. **52**, 434001 (2019).
[13]M. T. Hehner, D. Gatti, and J. Kriegseis, "Stokes-layer formation under absence of moving parts—A novel oscillatory plasma actuator design for turbulent drag reduction," Phys. Fluids **31**, 051701 (2019).
[14]H. Choi, P. Moin, and J. Kim, "Active turbulence control for drag reduction in wall-bounded flows," J. Fluid Mech. **262**, 75–110 (1994).
[15]M. Quadrio and P. Ricco, "Critical assessment of turbulent drag reduction through spanwise wall oscillations," J. Fluid Mech. **521**, 251–271 (2004).
[16]M. J. Walsh, "Riblets as a viscous drag reduction technique," AIAA J. **21**, 485–486 (1983).
[17]D. W. Bechert, M. Bruse, W. V. Hage, J. T. Van der Hoeven, and G. Hoppe, "Experiments on drag-reducing surfaces and their optimization with an adjustable geometry," J. Fluid Mech. **338**, 59–87 (1997).
[18]C. M. White and M. G. Mungal, "Mechanics and prediction of turbulent drag reduction with polymer additives," Annu. Rev. Fluid Mech. **40**, 235–256 (2008).
[19]W. McComb and L. Rabie, "Local drag reduction due to injection of polymer solutions into turbulent flow in a pipe. Part I: Dependence on local polymer concentration," AIChE J. **28**, 547–557 (1982).
[20]Y. Hou, V. Somandepalli, and M. Mungal, "Streamwise development of turbulent boundary-layer drag reduction with polymer injection," J. Fluid Mech. **597**, 31–66 (2008).
[21]F. E. Fish, "The myth and reality of gray's paradox: Implication of dolphin drag reduction for technology," Bioinspiration Biomimetics **1**, R17 (2006).
[22]Z. Dou, J. Wang, and D. Chen, "Bionic research on fish scales for drag reduction," J. Bionic Eng. **9**, 457–464 (2012).
[23]G. V. Lauder and E. G. Drucker, "Morphology and experimental hydrodynamics of fish fin control surfaces," IEEE J. Oceanic Eng. **29**, 556–571 (2004).
[24]F. E. Fish and G. V. Lauder, "Passive and active flow control by swimming fishes and mammals," Annu. Rev. Fluid Mech. **38**, 193–224 (2006).
[25]S. Xu, D. Rempfer, and J. Lumley, "Turbulence over a compliant surface: Numerical simulation and analysis," J. Fluid Mech. **478**, 11–34 (2003).
[26]J. H. Kim and J. H. Lee, "Skin-friction drag reduction in turbulent channel flow based on streamwise shear control," Int. J. Heat Fluid Flow **63**, 28–43 (2017).
[27]Z. Zhang, Q. Wang, and S. Zhang, "Review of computational fluid dynamics analysis in biomimetic applications for underwater vehicles," Biomimetics **9**, 79 (2024).
[28]X. Xue, S. Wang, H.-D. Yao, L. Davidson, and P. V. Coveney, "Physics informed data-driven near-wall modelling for lattice Boltzmann simulation of high Reynolds number turbulent flows," Commun. Phys. **7**, 338 (2024).
[29]P. J. Roache, "Perspective: A method for uniform reporting of grid refinement studies," J. Fluids Eng. **116**(3), 405–413 (1994).
[30]S. Hoyas and J. Jiménez, "Scaling of the velocity fluctuations in turbulent channels up to $re_\tau = 2000$," Phys. Fluids **18**, 011702 (2006).
[31]J. C. del Álamo, J. Jiménez, P. Zandonade, and R. D. Moser, "Scaling of the energy spectra of turbulent channels," J. Fluid Mech. **500**, 135–144 (2004).
[32]J. C. del Álamo and J. Jiménez, "Spectra of the very large anisotropic scales in turbulent channels," Phys. Fluids **15**, L41–L44 (2003).
[33]W.-X. Huang, S. J. Shin, and H. J. Sung, "Simulation of flexible filaments in a uniform flow by the immersed boundary method," J. Comput. Phys. **226**, 2206–2228 (2007).